Trapping of sub-relativistic particles in laser driven accelerators

Adi Hanuka[a] and Levi Schächter
Department of Electrical Engineering Technion–Israel Institute of Technology, Haifa 32000, Israel

(Received 16 September 2017; accepted 27 November 2017; published online 26 December 2017)

We investigate the longitudinal and transverse dynamics of sub-relativistic electrons during the trapping process, as facilitated by an adiabatically tapered dielectric structure. The characteristics of the trapped electrons are studied for different initial conditions and structure's parameters. A set of optimal parameters that exemplify our approach are presented. Specifically, we determine the condition where the transverse emittance is preserved during the trapping process. *Published by AIP Publishing*. https://doi.org/10.1063/1.5005031

I. INTRODUCTION

Laser driven accelerators bear inherent advantages over conventional microwave accelerators due to the reduction of 4–5 orders of magnitude in wavelength. Accordingly, the former have become an appealing alternative to the latter for both high energy physics[1,2] as well as for medical applications.[3] This trend is also strengthened by the fact that over the last decade there has been significant progress in wall-plug to light efficiency of lasers.[4–6]

Optical accelerators present a number of advantages over their microwave counterparts. Most notably, the reduction in wavelength facilitates a reduction in the length of the machine. An optical machine could be two orders of magnitude shorter than its RF counterpart.[7] For example, the 50 km long ILC machine could be readily accommodated in the 3 km SLAC tunnel.[8] Medical accelerators could be shrunk from 50 cm long to no more than a few centimeters.

Another appealing advantage of operating in the optical range is that higher accelerating gradients can be achieved.[9] Additionally, while in both microwave and optical machines, the accelerating gradient is limited by the material's ability to sustain an intense electric field, in microwave machines breakdown limits the gradient to 20–50 MV/m,[2,10,11] whereas in laser driven structures—most commonly made from dielectric materials[12]—gradients of 1–10 GV/m have been theoretically shown to be feasible[13] prior to breakdown.

Beyond size and gradient, accelerators are also tested by the number of accelerated particles. In microwave machines,[14,15] the typical bunch contains roughly 10^{10} electrons, and its dimensions are of the order of $\sigma_z \simeq 300\,\mu$m, $\sigma_x \simeq 10\,\mu$m, and σ_y is tens of nanometers; thus, the density is of the order of $n_{el} \simeq 5 \times 10^{19}\,\mathrm{cm}^{-3}$ at the interaction point (IP).

In contrast, in an optical machine, the volume needs to be a small fraction of the wavelength. Thus, assuming that the latter is $\lambda \simeq 1\,\mu$m, the bunch's dimensions should be $\sigma_z \simeq 0.1\lambda$, $\sigma_x \simeq \sigma_y \simeq 0.2\lambda$. Regarding density, in this study, our analysis considers a point which is away from the IP, and thus we assume a density 100 times lower than microwave machines, namely $n_{el} \sim 10^{18}\,\mathrm{cm}^{-3}$. As a result, a single bunch in an optical machine could contain 5000 electrons.

This number of accelerated charge should satisfy the luminosity constraint as well as the medical dose requirements.[3] In microwave machines, these are facilitated by a repetition rate of 5 Hz, number of bunches in train of ~2000, and 2×10^{10} electrons in one bunch[16]), resulting in $\sim 1 \times 10^{14}$ electrons per second. For optical machines, we assume a train of 10^3 bunches (3 ps) and a repetition rate of 25 MHz, and thus we anticipate a similar number of electrons per second as microwave machines.

From the operational perspective, the trapping process of sub-relativistic particles, governed by the trapping condition, also differs between microwave and optical machines. The condition for electron trapping[17] for a given initial velocity ($c\beta_{in}$) is a minimum accelerating field of $E_{min} = 2\pi(mc^2/e\lambda)\sqrt{(1-\beta_{in})/(1+\beta_{in})}$, considering a *uniform* acceleration structure, wherein the accelerating field (E) propagates at the speed of light.

In the case of initially slow electrons, the trapping constraint is several orders of magnitude higher if λ is in the optical range rather than microwave. Specifically, in microwave machines, wherein λ is of the order of centimeters and thus the typical value of the normalized longitudinal field $a = eE\lambda/mc^2$ is unity, the electrons become relativistic within a few wavelengths. In contrast, since in the optical regime $\lambda = 1\,\mu$m, the typical value of a is smaller than unity. As a result, electrons may only reach relativistic velocities after many wavelengths. For actual acceleration, the charge must be kept in synchronization with the accelerating field throughout the interaction length. In other words, the amplitude and the phase of the accelerating mode must be *tapered*.

Ample designs and studies have been conducted with regard to trapping electrons in microwave machines. However, to the best of our knowledge—a design of a tapered structure for trapping sub-relativistic electrons in an optical regime, as well as a thorough investigation of the trapping process properties—has not been conducted as yet.

In this study, we present a quasi-analytic formulation, as well as numerical studies, of the trapping dynamics of sub-relativistic particles in a tapered laser-driven acceleration structure, which serves as a booster. This formalism enables us to examine the interaction in phase-space and optimize it.

As a primary step, in order to maximize the trapping efficiency, the structure's longitudinal tapering is

[a]Adiha@tx.technion.ac.il

established.[18] This step is briefly presented in Sec. II as well as the envisaged configuration (shown in Fig. 1) and the model assumptions. Section III presents an analytical formulation of the longitudinal dynamics of the trapping process for a distribution of sub-relativistic particles. This is followed by the transverse dynamics of the trapping process, discussed in Sec. IV. Finally, in Sec. V, we examine the effect of the initial phase and energy distributions on the trapped electrons, and the latter's characteristics (energy spread and transverse emittance).

II. SYSTEM'S DESCRIPTION

Without significant loss of generality, throughout our analysis, we adopt a configuration of a dielectric-loaded cylindrical waveguide with a constant vacuum tunnel's radius (internal radius) as shown in Fig. 1. We assume that a single TM_{01} laser mode (shown in the red line) with a phase velocity β_{ph} is co-propagating with a single bunch (shown in solid blue). Throughout the analysis, we trace N electrons in one optical period, thus subject to the assumption that all the other periods experience, eventually, the same conditions—shown in dashed blue in Fig. 1.

The direction of propagation being the z-axis, the electromagnetic field components in the vacuum are

$$\begin{aligned} E_z(\rho,z) &= E_0(z) I_0(\Gamma\rho)\exp\left(-j\frac{\omega}{c\beta_{ph}}z\right) \\ E_r(\rho,z) &= j\gamma_{ph} E_0(z) I_1(\Gamma\rho)\exp\left(-j\frac{\omega}{c\beta_{ph}}z\right) \\ H_\phi(\rho,z) &= \frac{1}{\eta_0}\beta_{ph} E_r(\rho,z), \end{aligned} \tag{1}$$

where E_0 is the laser's amplitude, $\eta_0 = 377\Omega$ is the wave impedance, I_0, I_1 are the modified Bessel functions of the first kind, $\Gamma = \omega\sqrt{\beta_{ph}^{-2}-1}/c$, and ρ is the radial coordinate.

Additional model assumptions are as follows: (i) DC space charge effects are ignored. (ii) Since we are interested not only in the field's effect on the electrons' distribution, but also vice-versa, it is assumed that the relation between interaction impedance (Z_{int}) and the phase velocity is known.[18] Therefore, for a current I, we define a coupling coefficient $\alpha(\beta_{ph}) = eIZ_{int}(\beta_{ph})/mc^2$. Table I presents the configuration's parameters used for the numerical simulations throughout this study (unless otherwise specified). Additional structure's properties are discussed in Appendix A.

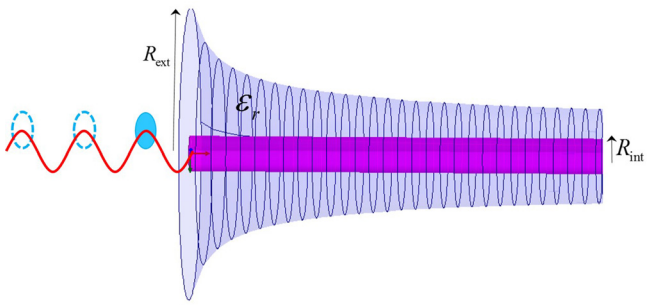

FIG. 1. Schematics of the envisaged configuration. Dielectric (ε_r) loaded cylinder waveguide with a constant vacuum channel (R_{int}). The tapered external radius (R_{ext}) matches between the phase velocity of the accelerating TM_{01} laser mode (red) to the co-propagating sub-relativistic electron beam (blue).

In what follows, we formulate the interaction dynamics between the laser wave and the ensemble of N electrons divided into M macro-particles. Longitudinal and transverse dynamics are presented in Secs. III and IV, respectively. In both Sections, it is assumed that the initial distribution of the ensemble in one laser period is known. The phase of the i-th particle χ_i is relative to the wave, its normalized energy is γ_i, and its radial location is ρ_i. Moreover, for the sake of designing the structure's longitudinal taper, namely determining how the phase velocity changes in space $(\beta_{ph}(\zeta))$, we adopt the *resonant particle* approach[17]—see Appendix B. The structure's longitudinal taper should satisfy the adiabaticity condition, in which the change in energy, $\Delta\gamma/(\gamma-1)$, in one laser period in the material, is of the order of unity or smaller.

III. LONGITUDINAL DYNAMICS

In the case of a tapered structure, ignoring the radial motion of the beam, the trapping dynamics is described by the following set of equations:[18]

$$\begin{cases} \dfrac{db}{d\zeta} = \sqrt{\alpha}\langle I_0(\Gamma\rho_i)\exp(-j\chi_i)\rangle_i \\ \dfrac{d\gamma_i}{d\zeta} = -\dfrac{1}{2}\left[\sqrt{\alpha}bI_0(\Gamma\rho_i)\exp(j\chi_i)+\text{c.c.}\right] \\ \dfrac{d\chi_i}{d\zeta} = 2\pi\left[\dfrac{1}{\beta_{z,i}}-\dfrac{1}{\beta_{ph}(\zeta)}\right], \end{cases} \tag{2}$$

where $\zeta \equiv z/\lambda$, $\langle\ldots\rangle_i = \frac{1}{M}\sum_{i=1}^{M}$, and c.c. represents the complex conjugate. The first equation describes the laser's normalized amplitude $(b \equiv eE_0\lambda/(\sqrt{\alpha}mc^2))$, and the second and third equations describe the energy (γ_i) and phase (χ_i) of the i-th electron located at radius ρ_i, with a longitudinal velocity $\beta_{z,i}$. Note that the global energy conservation is not altered due to the tapering

$$\frac{d}{d\zeta}\left[\langle\gamma_i\rangle_i + \frac{1}{2}|b|^2\right] = 0. \tag{3}$$

TABLE I. Parameters of the laser, structure, and electron beam. (*) The asterisk indicates that this current corresponds to 5000 electrons in one laser period.

Parameter	Symbol	Value
Laser wavelength (μm)	λ	2
Gradient on axis (GV/m)	E_0	1.8
Laser input power (MW)	P_{in}	2.1
Dielectric constant	ε_r	11.68
Structure's length (λ)	L	40
Number of macro-particles	M	360
Current (A)	I	0.047*
Initial electron energy (MeV)	E_{in}	0.045
Initial phase spread (%)	$\frac{\Delta\chi_{in}}{2\pi}$	5
Initial bunch length (fs)	Δt_b	0.85
Initial energy spread (10^{-3})	$\frac{\Delta\gamma_{in}}{\gamma_{in}-1}$	0.7

While the dependence of the capturing process [Eq. (2)] on the longitudinal coordinate was shown in our previous work,[18] we see it as imperative to present its dependence on the radial coordinate. In this section, we assume that the motion is confined by the strong magnetic field yet the transverse *location* of the particle is accounted for ($E_z \propto \mathrm{I}_0(\Gamma\rho)$).

Let us assume a cylindrical vacuum tunnel of radius $R_{\mathrm{int}} = 0.3\lambda$, and a uniform initial distribution of particles along the electron beam radius $R_{\mathrm{b}} = 0.3R_{\mathrm{int}}$. Since the accelerating gradient is higher towards the vacuum-dielectric interface, the first electrons to gain energy are the ones at the outer radii (bottom frame in Fig. 2). Next, along the first 20% of the waveguide, there are radial oscillations, whereas most of the beam continues gaining energy, some electrons close to the axis are left behind (middle frame in Fig. 2). Eventually, at the exit of the waveguide, most of the beam was accelerated to 6 MeV except the electrons in the vicinity of the axis (red circles in the top frame in Fig. 2). Those electrons have final kinetic energy which is smaller than 80% of the resonant particle final kinetic energy, and thus they were not trapped. As a result, at the exit of the structure the beam is radially non-uniform. We examined several additional trapping criteria as discussed in Appendix C.

While this dependence of the radius is also shown in Fig. 3, we would like to point out the impact of the initial energy. Figure 3 shows the final kinetic energy of the i-th electron normalized to the resonant particle final kinetic energy as a function of its initial uniform distribution $\gamma_{\mathrm{i,in}}$, and radial location ρ_i along the electron beam. Notably, the particles which were not trapped had an initial energy smaller than the resonant particle. Therefore, it is preferable to inject the beam with a slightly higher energy than the resonant particle's initial energy, for which the structure was designed.

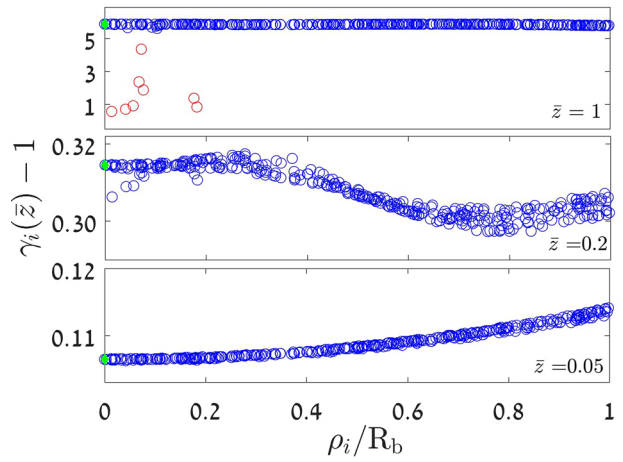

FIG. 2. Kinetic energy of the i-th electron for three frames during the capturing process along the structure ($\bar{z} = z/L = 0.05, 0.2, 1.0$) as a function of its radial location ρ_{i} in the electron beam ($R_{\mathrm{b}} = 0.3R_{\mathrm{int}}$, $R_{\mathrm{int}} = 0.3\lambda$). While the initial radial distribution is uniform, the electrons far from axis are the first to gain energy (bottom frame), then oscillating along the waveguide (middle frame), and eventually forming a radially non-uniform beam at the exit of the structure (top frame). The resonant particle is highlighted in green, the trapped electrons in blue, and the un-trapped electrons in red.

IV. TRANSVERSE DYNAMICS

In this section, we include the transverse motion in the absence of a guiding DC magnetic field (considered to be infinite in Sec. III).

As a result of the transverse motion, the effective electric field components are

$$\begin{aligned} E_{z,i}^{\mathrm{eff}} &= E_{z,i} + \beta_{r,i}\eta_0 H_{\phi,i} = E_{z,i} + \beta_{r,i}\beta_{\mathrm{ph}}E_{r,i} \\ E_{r,i}^{\mathrm{eff}} &= E_{r,i} - \beta_{z,i}\eta_0 H_{\phi,i} = \left(1 - \beta_{z,i}\beta_{\mathrm{ph}}\right)E_{r,i}, \end{aligned} \tag{4}$$

where $\beta_{r,i}$ is the particle's radial velocity. Therefore, the three equations of motion and energy equation for the i-th particle are

$$\begin{aligned} \frac{d\gamma_i}{d\zeta} &= -\frac{1}{2}\sqrt{\alpha}\left\{ b\left[I_0(\Gamma\rho_i) + j\frac{\beta_{r,i}}{\beta_{z,i}}\gamma_{\mathrm{ph}} I_1(\Gamma\rho_i)\right]\exp(j\chi_i) + \mathrm{c.c.}\right\} \\ \frac{d\gamma_i\beta_{z,i}}{d\zeta} &= -\frac{1}{2}\sqrt{\alpha}\left\{ b\frac{1}{\beta_{z,i}}\left[I_0(\Gamma\rho_i) + j\gamma_{\mathrm{ph}}\beta_{\mathrm{ph}}\beta_{r,i} I_1(\Gamma\rho_i)\right] \right. \\ &\qquad \left. \times\exp(j\chi_i) + \mathrm{c.c.}\right\} \\ \frac{d\gamma_i\beta_{x,i}}{d\zeta} &= -\frac{1}{2}\sqrt{\alpha}\Gamma x_i\left\{ jb\left(\frac{1}{\beta_{z,i}} - \beta_{\mathrm{ph}}\right)\gamma_{\mathrm{ph}}\frac{I_{\mathrm{c}}(\Gamma\rho_i)}{2}\exp(j\chi_i) + \mathrm{c.c.}\right\}, \end{aligned} \tag{5}$$

where $I_c(r) = 2I_1(r)/r$ if $r > 0$, and 1 if $r = 0$, $\rho_i = \sqrt{x_i^2 + y_i^2}$, and $\beta_{r,i} = (\beta_{x,i}x_i + \beta_{y,i}y_i)/\rho_i$. Similar equation for $\beta_{y,i}$ as for $\beta_{x,i}$ is facilitated by replacing x_i with y_i, respectively, in the third equation in Eq. (5).

While the phase equation in Eq. (2) remains the same, the energy conservation law constrains the laser's amplitude equation to be

$$\frac{\mathrm{d}b}{d\zeta} = \sqrt{\alpha}\langle\left[I_0(\Gamma\rho_i) - uI_1(\Gamma\rho_i)\right]\exp\left(-j\chi_i\right)\rangle_i, \tag{6}$$

where $u \equiv j\gamma_{\mathrm{ph}}\beta_{r,i}/\beta_{z,i}$. Therefore, together with

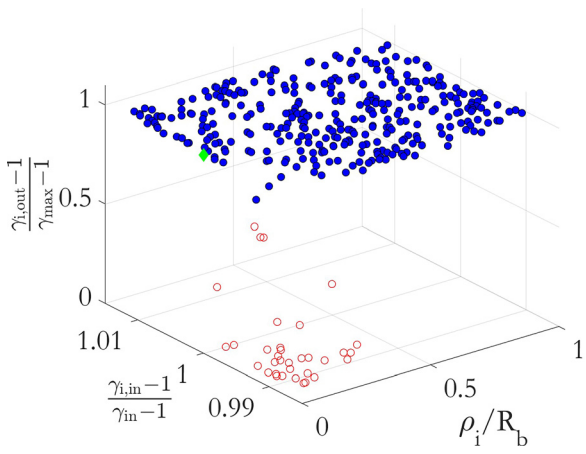

FIG. 3. Final kinetic energy of the i-th electron normalized to the resonant particle's (green) final kinetic energy as a function of the i-th electron's initial uniform distribution $\gamma_{\mathrm{i,in}}$, and radial location ρ_i in the electron beam radius R_{b}. Notably, as compared with trapped electrons (blue), the untrapped electrons (red) are the ones closer to the center of the beam and have an initial energy smaller than the resonant particle.

$$\frac{dy_i}{d\zeta} = \frac{\beta_{y,i}}{\beta_{z,i}}; \qquad \frac{dx_i}{d\zeta} = \frac{\beta_{x,i}}{\beta_{z,i}}. \tag{7}$$

Equations (5)–(7) form the full set of equations for establishing the transverse dynamics.

A flavor of a solution is given in Fig. 4 for the parameters in Table I, and $R_{\text{int}} = 0.3\lambda$, $R_{\text{b}} = 0.07R_{\text{int}}$. It is assumed that all particles are initially distributed uniformly in energy, phase, and radial location, and the initial transverse emittance is $\sim 10^{-11}$ m. The output energy of the particles as a function of the phase and radial location is presented in Figs. 4(a) and 4(b), respectively. In both figures, the resonant particle is highlighted in green. The bottom two figures describe the dynamics along the structure in terms of the mean velocity of the bunch Fig. 4(d), and emittance and energy conservation Fig. 4(c).

First, it is evident that the particles are assorted into three groups as shown in Fig. 4(a): (i) *trapped* particles (blue circles)—for which the final kinetic energy is higher than 80% of the resonant particle's final kinetic energy, (ii) *untrapped* particles (red circles), and (iii) *stuck* particles (black squares)—which hit the structure's wall.

Second, the trapped accelerated particles are those in the vicinity of the accelerating phase of $\chi = \pi$. Notably, the trapped bunch is not centered around π, but rather the electrons in the $\pi + 0$ region are most likely to be accelerated. Also, as shown in Fig. 4(b), the particles closer to the axis were not accelerated. Figure 4(c) shows that the change in the longitudinal mean velocity of all the particles along the structure is adiabatic. Figure 4(d) shows the evolution of the emittance, which is several orders of magnitude higher than the global energy conservation defined in Eq. (3).

Evidently, it is critical to reduce the number of stuck particles as much as possible and maximize the number of trapped particles. In order to achieve these requirements, we operate in short structures (less than 50 optical cycles). However, in many cases, it is yet insufficient; therefore, increasing the internal radius is inevitable. In Appendix D, we investigate the impact of the internal radius of the structure, taking the initial emittance to be zero.

V. DISCUSSION

Special attention should be given to the emittance. In particular, it is important to establish the conditions that the transverse emittance at the input is not ruined by the trapping process. For the purpose of trapping all the particles, we adopt a structure's radius of $R_{\text{int}} = 0.5\lambda$ and a focused beam. Varying the transverse emittance at the *input* $(\epsilon_{\perp,\text{in}})$, it is possible by changing either the beam radius R_{b} or the mean transverse velocity of all particles $\sqrt{<\beta_{\perp}^2>}$—see Fig. 5(a). For each set of initial conditions, the *output* transverse emittance $(\epsilon_{\perp,\text{out}})$ of the trapping process is presented in Fig. 5(b).

As could be inferred from these two figures, for the same initial transverse emittance [$\epsilon_{\perp,\text{in}} = 0.08$ nm for points 1–3 in Fig. 5(a)], the output transverse emittance of the trapped particles could be an order of magnitude different [$\epsilon_{\perp,\text{in}} \simeq 0.6, 0.1, 1.5$ nm, respectively, for points 1, 2, and 3

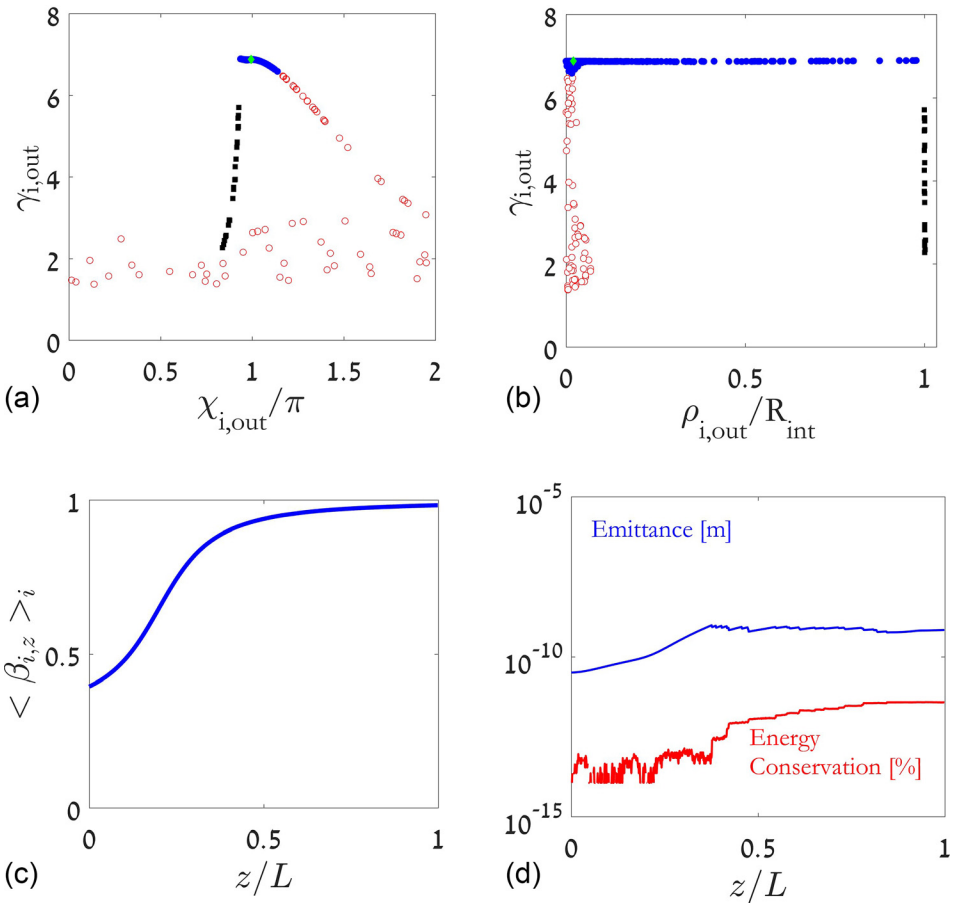

FIG. 4. An example of the dynamics for $R_{\text{int}} = 0.3\lambda$ and $R_{\text{b}} = 0.07R_{\text{int}}$ considering the transverse motion. The electrons' output energy is presented as a function of the output phase [in (a)], and as a function of the output radial coordinate [in (b)], whereas the dynamics of the longitudinal mean velocity of all the particles, and their transverse emittance along the structure ($L = 40\lambda$) is described in (c) and (d), respectively. In the top two frames, the resonant particle is highlighted in green, the trapped electrons in blue, the un-trapped electrons in red, and the stuck electrons in black squares.

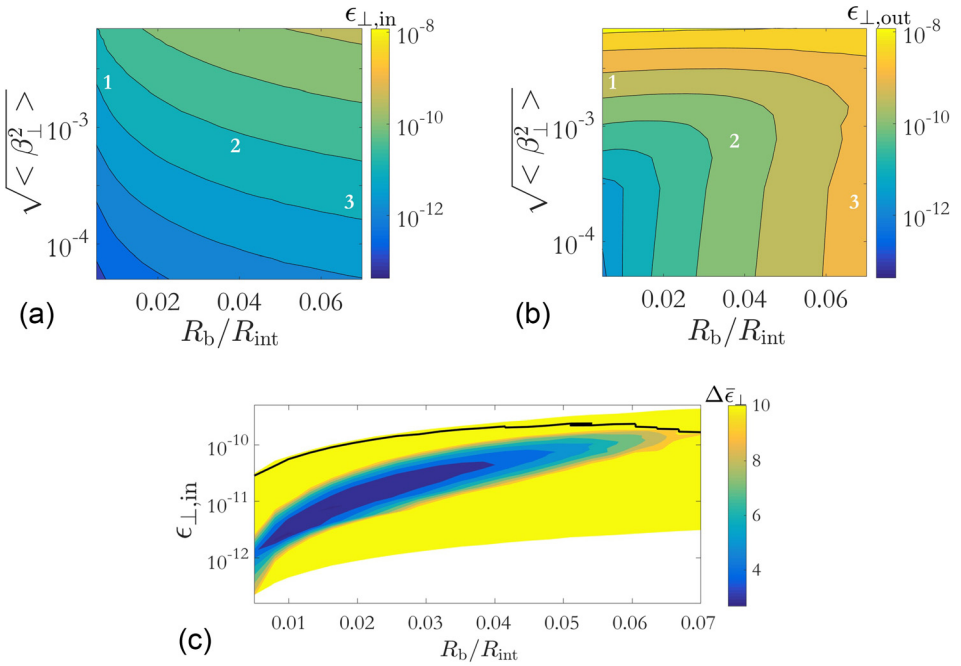

FIG. 5. Contours of transverse emittance (a) for *all* particles at the input and (b) for *trapped* particles at the output for $R_{\mathrm{int}} = 0.5\lambda$, and a range of values of beam radius R_b and initial velocity β_r. (c) The emittance growth of *trapped* particles shows that there is a combination of initial conditions, so that all particles are trapped and their final transverse emittance is preserved. The area above the bold black line represents events in which either not all the particles were trapped or particles were stuck.

in Fig. 5(b)]. This is due to a different effect of the mean transverse velocity and beam radius on the trapping. In order to better understand the emittance evolution, we define the transverse emittance growth

$$\Delta\bar{\epsilon}_\perp = \frac{\epsilon_{\perp,\mathrm{out}} - \epsilon_{\perp,\mathrm{in}}}{\epsilon_{\perp,\mathrm{in}}}. \tag{8}$$

Figure 5(c) shows the transverse emittance growth ($\Delta\bar{\epsilon}_\perp$) as a function of beam radius and an initial transverse emittance. The inner contour in this figure implies that there is a combination of initial conditions, so that all particles are trapped and their final transverse emittance is virtually preserved. The area below the bold black line represents events in which all particles were trapped. Therefore, in all other events (above the black line), regardless of the input transverse emittance, the transverse velocity was too high, and it was inevitable that some of the particles hit the structure.

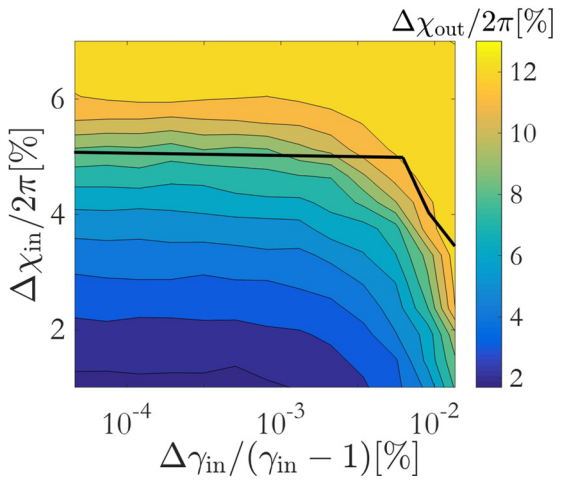

FIG. 6. Output phase spread of trapped particles as a function of the initial energy spread and phase spread. The area above the black bold line represents simulations where not all particles were trapped.

Please note that the numerical results presented in Fig. 5 for the parameters in Table I are an average over 20 simulations for each input parameters (R_b, $\sqrt{<\beta_\perp^2>}$), while the initial energy, energy spread, and phase spread remain the same; the error for each simulation is smaller than 10^{-14} [%].

Next, we investigate the impact of the initial energy spread $\Delta\gamma_\mathrm{in}/(\gamma_\mathrm{in}-1)$ and phase spread $\Delta\chi_\mathrm{in}/2\pi$ on the trapping process and its properties. According to Fig. 5(c), we choose a combination of initial conditions ($R_{\mathrm{int}} = 0.5\lambda$, $R_\mathrm{b} = 0.03$ R_{int}, $\epsilon_{\perp,\mathrm{in}} \simeq 0.02$ nm) so that all particles are trapped and their final transverse emittance is preserved for the initial energy and phase spread given in Table I.

It is evident that by varing $\Delta\gamma_\mathrm{in}$ and $\Delta\chi_\mathrm{in}$, the final kinetic energy and mean phase of trapped particles remain virtually the same. Moreover, while the initial energy spread changes by orders of magnitude, the final energy spread of the trapped particles does not change significantly—being the same characteristic as we previously[18] showed for the longitudinal motion alone.

In contrast, the number of trapped particles (M_Trap) and their phase spread ($\Delta\chi_\mathrm{out}$) do vary quite significantly. The latter quantity (averaged over 20 simulations) is shown in Fig. 6 as a function of the initial energy spread and initial phase spread. Notably, for energy spread values smaller than 6×10^{-3}, the capturing process is more sensitive to the phase spread rather than the initial energy spread. The area above the black bold line represents simulations where not all particles were trapped.

Figure 6 shows that the output phase spread of the *trapped* particles increases for larger initial phase spread. For example, for energy spread values smaller than 6×10^{-3}, a tightly pre-bunched beam of $\Delta\chi_\mathrm{in}/2\pi = 1\%$ would result in relatively the same phase spread of the trapped beam at the output. However, slightly wider spread of $\Delta\chi_\mathrm{in}/2\pi = 2\%$ would result in a trapped beam of $\Delta\chi_\mathrm{out}/2\pi = 4\%$ at the output (two times wider). Evidently,

TABLE II. Parameters for optimal operation, whereby all particles are trapped and their transverse and longitudinal emittance are conserved.

Parameter	Symbol	Value
Vacuum channel radius (μm)	R_{int}	1
Electron beam radius (nm)	R_{b}	30
Input transverse emittance (nm)	$\epsilon_{\perp,\mathrm{in}}$	0.02
Initial phase spread (%)	$\frac{\Delta\gamma_{\mathrm{in}}}{2\pi}$	≤ 5
Initial energy spread (10^{-3})	$\frac{\Delta\gamma_{\mathrm{in}}}{\gamma_{\mathrm{in}}-1}$	≤ 6

if the energy spread is higher than 6×10^{-3}, the output phase spread increases significantly even for an initially small phase spread. Table II summarizes the parameters required for optimal operation, whereby all particles should be trapped while conserving their transverse and longitudinal emittance.

VI. CONCLUSION

We presented a quasi-analytic formulation of the longitudinal and transverse dynamics of sub-relativistic electrons in an adiabatically tapered laser-based acceleration structure. We showed the trapping process of an ensemble of electrons and discussed several ways to improve its properties, for example, reducing the number of particles hitting the structure's wall, and preserving the transverse emittance of the trapped particles.

We further investigated the trapping process as a function of the electrons' initial conditions—initial energy, energy spread, and phase spread. This study allows us to define a set of parameters for both the accelerating structure and the sub-relativistic electron beam resulting in an optimal operation—see Table II. Specifically, we determine the conditions under which the transverse emittance is preserved during the trapping process.

ACKNOWLEDGMENTS

This study was supported by the Israel Science Foundation and the Rothschild Caesarea Foundation.

APPENDIX A: PROPERTIES OF THE ENVISAGED STRUCTURE

In this appendix, we present the structure's group velocity (β_{gr}) and coupling parameter's (α) dependence on the dielectric constant (ε_{r}) and the cylinder's internal radius (R_{int}).

In order to calculate the group velocity, we derive the homogeneous dispersion relation given by

$$D_H(\omega, k_z) = \varepsilon_r T_1(\Lambda R_{\mathrm{int}}) I_0(\Gamma R_{\mathrm{int}}) + \frac{\Lambda}{\Gamma} T_0(\Lambda R_{\mathrm{int}}) I_1(\Gamma R_{\mathrm{int}}), \tag{A1}$$

where $k_z = \omega/(c\beta_{\mathrm{ph}})$, $\Gamma = \sqrt{k_z^2 - (\omega/c)^2}$ and $\Lambda = \sqrt{\varepsilon_r(\omega/c)^2 - k_z^2}$, K_0 and I_0 are the modified Bessel functions of the first and second kind, respectively, $T_0(\Lambda r) \equiv J_0(\Lambda r)\ Y_0(\Lambda R_{\mathrm{ext}}) - J_0(\Lambda R_{\mathrm{ext}}) Y_0(\Lambda r)$, $T_1(\Lambda r) \equiv -J_1(\Lambda r)\ Y_0(\Lambda R_{\mathrm{ext}}) + J_0(\Lambda R_{\mathrm{ext}}) Y_1(\Lambda r)$ and J_n and Y_n are the n-th order Bessel functions of the first and second kind, respectively.

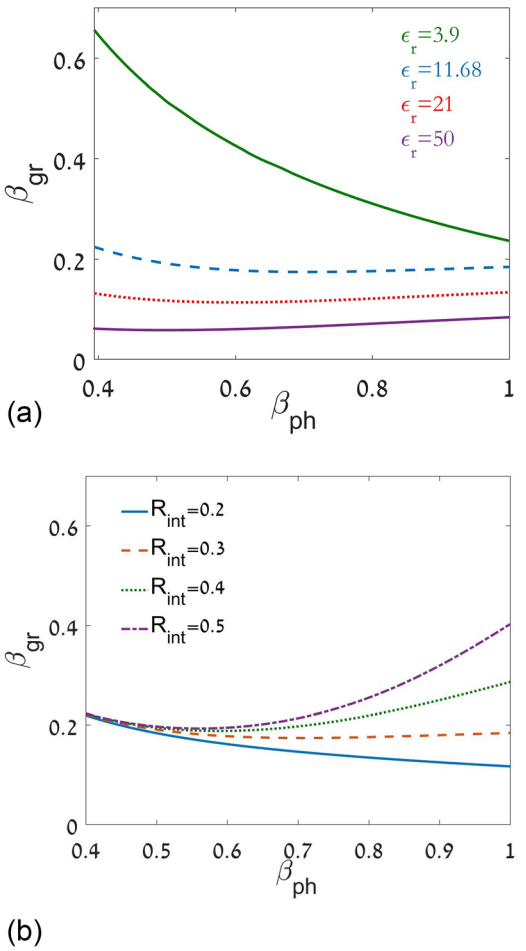

FIG. 7. Group velocity as a function of the phase velocity for (a) $R_{\mathrm{int}} = 0.3\lambda$ and various dielectric coefficients, and (b) $\varepsilon_{\mathrm{r}} = 11.68$ and various vacuum core radii.

For a given dielectric coefficient and internal radius, the external radius is locally established as a function of the phase velocity by solving Eq. (A1), and then the group

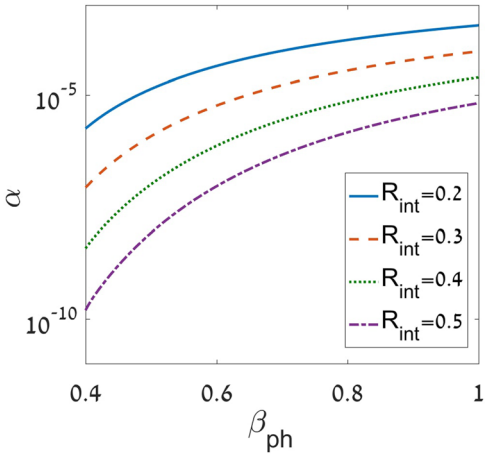

FIG. 8. Coupling parameter α as a function of the phase velocity for various vacuum core radii, and $\varepsilon_{\mathrm{r}} = 11.68$.

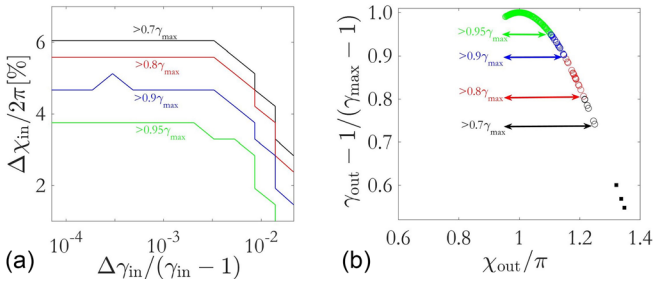

FIG. 9. (a) Contours of 100% trapped particles as a function of the initial energy spread and phase spread for four trapping criteria: 95% (green), 90% (blue), 80% (red), and 70% (black). (b) Output kinetic energy normalized to the maximum kinetic energy as a function of the output phase spread for input parameters of $\Delta\gamma_{in}/(\gamma_{in}-1)=2\times10^{-3}$ and $\Delta\chi_{in}/2\pi=0.065$.

velocity is derived. Figure 7(a) plots the group velocity for various dielectric coefficients given a fixed internal radius, whereas Fig. 7(b) plots the group velocity for various internal radii given a fixed dielectric coefficient. It is evident that the same group velocity can be achieved for various choices of ϵ_r, R_{int}. Moreover, the group velocity is nearly constant for the high dielectric coefficient.

With regards to the coupling factor, defined as $\alpha(\beta_{ph})=eIZ_{int}(\beta_{ph})/mc^2$, where I is the current, Fig. 8 shows that the coupling could vary in orders of magnitude as a function of the internal radius and the phase velocity.

APPENDIX B: RESONANT PARTICLE VERSUS ADAPTIVE DESIGN

For the sake of designing the structure's longitudinal taper, namely determining how the phase velocity changes in space ($\beta_{ph}(\zeta)$), we present two approaches: (i) resonant particle[17] and (ii) adaptive design.

In the first approach, we assume that all the charge is concentrated in one macro-particle (subscript r) on axis, and retains a constant acceleration phase, namely $d\chi_r/d\zeta=0$. In the second approach, we consider the initial distribution of the beam, and at each step, along the structure the phase velocity is evaluated based on the averaged phase, i.e., $d\langle\chi_i\rangle_i/d\zeta=0$. Therefore, the phase velocity is equal to the *average* velocity of all the particles, i.e., $\beta_{ph}=1/\langle\beta_{z,i}^{-1}\rangle_i$.

For a point charge ($R_b\to0$), adaptive design results in higher % of trapped particles with smaller energy spread. However, for a pancake beam (R_b is finite), the resonant particle approach results in all trapped particles as compared with zero trapped in the adaptive design approach.

APPENDIX C: TRAPPING CRITERION

In this appendix, we discuss several trapping criteria for various initial energy spread and initial phase spread. Throughout our analysis, we adopt the trapping criterion to be a final electron kinetic energy that is higher than 80% of the resonant particle's final energy (for which the structure was designed), namely $\gamma_{i,out}\geq0.8\gamma_{max}$. However, we examined a few other trapping criteria, such as 70%, 90%, and 95% of the resonant particle's final energy.

Figure 9 plots the desired case in which all the particles are trapped for different values of initial phase and energy spread ($R_{int}=0.5\lambda$, $R_b=0.03R_{int}$, and zero initial emittance). Each curve in 9a represents a different trapping criterion (70%, 80%, 90%, and 95% of the resonant particle's final energy); each curve represents the upper limit on the combination of initial conditions (energy spread and phase spread) that still allow the trapping of all particles.

Evidently, the output phase spread for each criterion will be different even for the same initial conditions. For example, for $\Delta\gamma_{in}/(\gamma_{in}-1)=2\times10^{-3}$ and $\Delta\chi_{in}/2\pi=0.065$, Fig. 9(b) shows the output energy normalized to the maximum output energy as a function of the output phase spread. The colors of the circle markers correspond to trapped particles according to different trapping criteria as in Fig. 9(a): 95% (green), 90% (blue), 80% (red), and 70% (black). The un-trapped particles are marked in black squares. Therefore, the effective phase spread (bunch length) grows as we consider lower kinetic energy for the particles to be regarded as trapped.

APPENDIX D: TRANSVERSE DYNAMICS' DEPENDENCE ON THE STRUCTURE'S VACUUM CLEARANCE

In this appendix, we investigate the impact of the internal radius of the structure, taking the initial emittance to be zero (the impact of non-zero initial emittance is discussed in Sec. V). We show that increasing the structure's vacuum tunnel results in higher output energy and less stuck particles. It is assumed that for all the radii, the structure's length is the same (40λ).

The output kinetic energy of the trapped particles is higher for wider vacuum clearance and is independent on the beam radius. For example, for $R_{int}/\lambda=0.3,0.4,0.5$, the output energy is $\gamma_{out}=7,20,55$, respectively. This occurs since for wider vacuum tunnel the structure's taper varies faster than for small vacuum clearance. Therefore, the particle is trapped faster and the remainder of the structure serves as a pure accelerating section, resulting in higher output kinetic

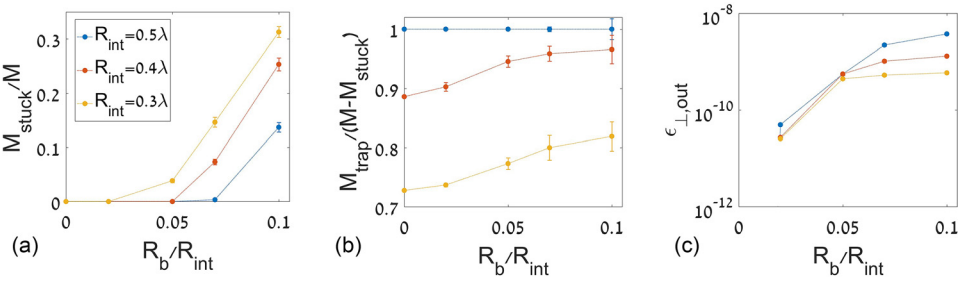

FIG. 10. Dynamics' properties as a function of the beam radius for $L=40\lambda$ and three values of the structure's internal radius R_{int}. As the internal radius is increased, the fraction of (a) stuck particles decreases (b) the fraction of trapped particles increases, (c) the latter's transverse emittance increases as well.

energy. Moreover, wider vacuum tunnel facilitates higher group velocity—as was shown in Appendix A—and as a result, the filling time of the structure decreases.

Figure 10 shows the following properties as a function of the beam radius, for three internal radii: (10a) percentage of stuck particles, (10b) percentage of trapped particles, and their (10c) output emittance. For zero initial emittance, internal radius $R_{\text{int}} = 0.5\lambda$ and beam radius $R_{\text{b}} \leq 0.07R_{\text{int}}$, the figure reveals not only that none of the particles are stuck but that all of them are trapped. Also, as the beam radius is bigger, the phase spread and energy spread remain nearly the same (less than 5%), whereas the emittance of the trapped particles is higher [Fig. 10(c)].

[1]J. Brau, Y. Okada, and N. Walker, "International linear collider reference design report, ILC global design effort and world wide study," Tech. Rep. **1** (2007).
[2]J. T. Seeman, "The Stanford linear collider," Annu. Rev. Nucl. Part. Sci. **41**, 389–428 (1991).
[3]R. J. England, R. J. Noble, B. Fahimian, B. Loo, E. Abel, A. Hanuka, and L. Schächter, in *Proceedings of the AAC14* (2014).
[4]G. D. Goodno, L. D. Book, and J. E. Rothenberg, Opt. Lett. **34**, 1204 (2009).
[5]D. J. Richardson, J. Nilsson, and W. A. Clarkson, JOSA B **27**, B63–B92 (2010).
[6]P. F. Moulton, G. A. Rines, E. V. Slobodtchikov, K. F. Wall, G. Frith, B. Samson, and A. L. G. Carter, IEEE J. Sel. Top. Quantum Electron. **15**, 85 (2009).
[7]R. J. England *et al*., Rev. Mod. Phys. **86**, 1337 (2014).
[8]K. P. Wootton, J. Mcneur, and K. J. Leedle, Rev. Accel. Sci. Technol. **9**, 105–126 (2016).
[9]K. Wootton, Z. Wu, B. Cowan, A. Hanuka, I. Makasyuk, E. Peralta, K. Soong, R. Byer, and R. England, Opt. Lett. **41**, 2696–2699 (2016).
[10]E. G. H. Hoffstaetter, S. M. Gruner, and M. Tigner, "Cornell energy recovery linac," Science Case and Project Definition Design Report (2013).
[11]L. Schächter, Phys. Rev. E **70**, 016504 (2004).
[12]A. Hanuka, L. Schächter, K. P. Wootton, Z. Wu, K. Soong, I. V. Makasyuk, and R. J. England, Proc. IPAC **16**, 1 (2016).
[13]A. Hanuka and L. Schächter, High Power Laser Sci. Eng. **2**, e24 (2014).
[14]H. Baer, T. Barklow, K. Fujii, Y. Gao, and A. Hoang, preprint arXiv:13066352 (2013).
[15]H. Braun, R. Corsini, J. Delahaye, A. D. Roeck, S. Doebert, G. Geschonke, A. Grudiev, C. Hauviller, B. Jeanneret, E. Jensen *et al*., CLIC-Note **764**, 1–41 (2008).
[16]N. Phinney, ICFA Beam Dyn. Newslett. **42**, 7–29 (2007).
[17]L. Schächter, in *Beam-Wave Interaction in Periodic and Quasi-Periodic Structures*, Particle Acceleration and Detection (Springer, Berlin/Heidelberg, 2011).
[18]A. Hanuka, C. Cohen, H. Lyabock, and L. Schächter, AIP Conf. Proc. **1812**, 100014 (2017).